

# Intermittent hydrodynamic jets in collapsars do not produce GRBs

Ore Gottlieb<sup>\*</sup>, Amir Levinson, Ehud Nakar

*School of Physics and Astronomy, Tel Aviv University, Tel Aviv 69978, Israel*

16 April 2021

## ABSTRACT

Strong variability is a common characteristic of the prompt emission of gamma-ray bursts (GRB). This observed variability is widely attributed to an intermittency of the central engine, through formation of strong internal shocks in the GRB-emitting jet expelled by the engine. In this paper we study numerically the propagation of hydrodynamic jets, injected periodically by a variable engine, through the envelope of a collapsed star. By post-processing the output of 3D numerical simulations, we compute the net radiative efficiency of the outflow. We find that all intermittent jets are subject to heavy baryon contamination that inhibits the emission at and above the photosphere well below detection limits. This is in contrast to continuous jets that, as shown recently, produce a highly variable gamma-ray photospheric emission with high efficiency, owing to the interaction of the jet with the stellar envelope. Our results challenge the variable engine model for hydrodynamic jets, and may impose constraints on the duty cycle of GRB engines. If such systems exist in nature, they are not expected to produce bright gamma-ray emission, but should appear as X-ray, optical and radio transients that resemble a delayed GRB afterglow signal.

**Key words:** transients: gamma-ray burst | hydrodynamics | methods: numerical | radiation mechanisms: general

## 1 INTRODUCTION

The prompt GRB emission exhibit variability over a vast range of timescales - from milliseconds to seconds (McBreen et al. 1994; Li & Fenimore 1996; Norris et al. 1996; Ramirez-Ruiz & Fenimore 1998, 2000; Nakar & Piran 2002a,b), with a large scatter of characteristics across sources. This observed variability may reflect an intermittent activity of the central engine (e.g. Levinson & Eichler 1993; Sari & Piran 1997; MacFadyen & Woosley 1998; Fenimore et al. 1999; Aloy et al. 2000; Lin et al. 2016), may result from the interaction between the jet and the medium into which it is launched (e.g. Aloy et al. 2002; Matzner 2002; Morsony et al. 2007; Gottlieb et al. 2019, hereafter GLN19), or both.

Recently, we have shown (GLN19) that under conditions anticipated in most GRBs, continuous injection of a hydrodynamic jet leads to an efficient photospheric emission, owing to a strong dissipation of the flow at a collimation shock which is located at a large distance from the jet injection point (roughly the stellar radius in long GRBs or the edge of the merger ejecta in short GRBs). The analysis of GLN19 further confirms that the photospheric efficiency of individual fluid elements is very sensitive to their baryon load; relatively low-loaded elements with terminal Lorentz factor  $\Gamma \gtrsim 100$  show high photospheric efficiencies, while more heavily loaded elements with lower Lorentz factors show low efficiencies. The 3D numerical simulations performed in GLN19 also indicate that the jet-medium interaction induces a rapid onset of the Rayleigh-Taylor instability, as previously found (Meliani & Keppens 2010; Matsumoto & Masada 2013a,b, 2019; Matsumoto et al. 2017; Toma et al. 2017; Gourgouliatos & Komissarov 2018), which in turn gives rise to a strong mixing of jet and cocoon material. This sporadic mixing re-

sults in large variations in the baryon loading of the different fluid elements, which in turn leads to large variations in the radiative efficiency that is seen as rapid variability of the photospheric emission. While the mixing enhances the mean baryon load on jet streamlines, the Lorentz factor within the jet core (a few degrees) was found to be still large enough ( $\Gamma > 100$ ) in all cases explored to allow a high average efficiency (albeit with large fluctuations) of the photospheric emission. However, energy dissipation near the photosphere by internal shocks that form in the mixing process has been found to be rather small, and the question whether it can significantly modify the emergent spectrum remains open.

Considerable dissipation near or above the photosphere in a weakly magnetized outflow seems to require the formation of strong internal shocks by intermittency of the central engine (in difference from reconnection in a Poynting jet). Such intermittency is also naively anticipated on physical grounds, as it is difficult to envision a steady operation of the engine over times vastly longer than the dynamical time. Since the outflow must break out of the confining medium prior to emitting, the question arises as to how the modulations produced by the engine evolve as they propagate through the surrounding medium. In this paper we address this question by performing 3D numerical simulations of GRB jets with periodic injection.

Previous works (Morsony et al. 2010; López-Cámara et al. 2014; Geng et al. 2016; Parsotan et al. 2018) attempted to compute the structure and emission of a modulated outflow by performing 2D simulations. However, axisymmetric simulations are known to be prone to severe numerical artifacts and, therefore, results based on such simulations cannot be trusted. In particular, the aforementioned mixing is absent in 2D simulations by virtue of the complete suppression of non-axisymmetric instabilities (see e.g. discussion in GLN19). Full 3D simulations of intermittent jet launching were per-

\* oregottlieb@mail.tau.ac.il

formed recently by [Lopez-Camara et al. \(2016\)](#). They found that shorter periodicity of the engine leads to heavier baryon loading and, consequently, lower terminal Lorentz factor. However, their simulation box extends only up to several stellar radii, much below the photosphere, and it is unclear from their results how the loading affects the prompt emission.

Here we perform 3D RHD simulations of modulated outflows, with modulation periods much shorter than the breakout time from the star, and follow their propagation from the injection radius, well within the star, up to several stellar radii. The output of the 3D simulations is then used to propagate the flow, using 2D simulations, to the vicinity of the photosphere. We find that such short modulations induce, quite generally, a substantially larger mixing of jet and stellar material along the jet axis than in the case of a continuous jet. This overloading of the jet pushes the photosphere to radii much larger than the dissipation radius of internal shocks generated by collisions of fast and slow shells, leading to extremely small (practically zero) radiative efficiency. We thus conclude that intermittent engines that expel hydrodynamic flows cannot produce the observed GRBs. If such systems exist in nature they should appear as X-ray, optical and radio transients that resemble GRB afterglows starting an hour or so after the burst.

## 2 NUMERICAL SETUP

We perform 3D RHD simulations of long GRB jets with an intermittent injection (see table 1). In all shown simulations a top-hat jet with an initial opening angle  $\theta_0 = 8^\circ$  and a cylindrical radius  $r_0 = 10^8$  cm is injected from  $z_{\text{beg}} = r_0/\theta_0 = 7 \times 10^8$  cm. The Lorentz factor and enthalpy per baryon at the injection boundary are, respectively,  $\Gamma_0 = 5$  and  $h_0 = 100$  at all times, such that the terminal Lorentz factor is limited to  $\eta_0 \equiv h_0\Gamma_0 = 500$ . The jet power is varied by changing the density at the injection boundary. To be concrete, the power is given by  $L_j(t) = \rho_{j0}(t)h_0\Gamma_0^2\beta_0(\pi r_0^2)c^3$ , where the injected density  $\rho_{j0}(t)$  is a periodic square wave in models *A*–*C* and *E*–*G*, with period and amplitude as given in table 1, and is a square of a sinusoidal function in model *D*. Our reference model *H* corresponds to a continuous jet injection with a power equals to the mean of that of models *E* and *G*. The jet is launched into a static non-rotating star with a mass of  $M = 10M_\odot$ , radius of  $R_* = 10^{11}$  cm and a density profile  $\rho(r) \propto r^{-2}x^3$ , where  $x \equiv (R_* - r)/R_*$ . We remind the reader that the product  $\eta = h\Gamma$  is conserved along streamlines of an adiabatic hydrodynamic flow (including across shock fronts). Consequently, in the absence of baryon loading and/or radiative losses it must remain constant. In our analysis, any reduction in  $\eta$  along streamlines indicates local mass entrainment. Thus, in what follows we use  $\eta$  as a measure for mixing (see GLN19 for further details).

Our 3D simulation grids end at  $5R_*$ . Since fresh elements show less baryon loading over time (GLN19), we continue the simulations after the jet head reaches  $5R_*$  to study the temporal evolution of the mixing in new jet elements. For models *E* and *G*, which hold observational promise, we trace the elements further, up to  $100R_*$ . For that purpose, we convert our 3D grids to 2D once the jet head reaches the edge of the 3D simulation box (see method in [Gottlieb et al. 2018](#)). At this point we stop the injection of the jet so that the jet length is  $5R_*$ . We stress that above  $z = 5R_*$  2D artifacts are not expected to have a substantial effect on the jet evolution ([Gottlieb et al. 2018](#)).

The 3D grids are Cartesian and identical to each other. We use three patches along the  $x$  and  $y$  axes, and one patch on the  $z$ -axis along which the jet propagates. The inner  $x$  and  $y$  axes are in the inner

Model	$f(t)$	$T$ [s]	$L_{\text{max}}$ [ $10^{50}$ erg]	$L_{\text{min}}$ [ $10^{50}$ erg]
<i>A</i>	$\Theta(t)$	0.2	1.0	0
<i>B</i>	$\Theta(t)$	2.0	1.0	0
<i>C</i>	$\Theta(t)$	4.0	1.0	0
<i>D</i>	$\sin^2(t)$	2.0	1.0	0
<i>E</i>	$\Theta(t)$	0.2	1.0	0.2
<i>F</i>	$\Theta(t)$	2.0	1.0	0.1
<i>G</i>	$\Theta(t)$	2.0	1.0	0.2
<i>H</i>	$\Theta(t)$	$\infty$	0.6	0.6

**Table 1.** The configurations of the simulations.  $f(t)$  is the injected periodic function: Heaviside step-function  $\Theta(t)$  or  $\sin^2(t)$ ,  $T$  is the duty cycle time, and  $L_{\text{max}}$  ( $L_{\text{min}}$ ) are the maximal (minimal) injected luminosity

$[7.5 \times 10^8 \text{ cm}]$  with 60 uniform cells. The outer patches are stretched logarithmically to  $[1 \times 10^{11} \text{ cm}]$  with 120 cells on each side. The  $z$ -axis has one uniform patch from  $z_{\text{beg}}$  to  $5R_*$  with 4000 cells. The total number of cells is therefore  $300 \times 300 \times 4000$ . The 2D grids are cylindrical with the  $r$  axis having the same resolution as the  $x$  and  $y$  axes in the 3D. The  $z$  axis is extended to  $10^{13}$  cm while keeping the same cell resolution, i.e. 80,000 uniform cells from  $z_{\text{beg}}$  to  $100R_*$ . The total number of cells is therefore  $300 \times 80000$ . Convergence tests are shown in Appendix A.

## 3 HYDRODYNAMICS

All simulations were run for times much longer than the breakout time, up to a point at which no significant change in the evolution of newly ejected shells is seen in each case. In all models we find that intermittent jet injection leads to excessive loading of the jet by mixing relative to the reference model, *H*, where the jet is injected continuously. This is seen in Figure 1, where  $\eta$  profiles along the jet axis are plotted at the end of the simulation time (as indicated in each panel)<sup>1</sup>.

The excessive mixing in intermittent jets seems to be a result of a different mixing process than the one seen in a continuous jet, as we explain below. When a continuous jet propagates in the dense medium (before it breaks out), a forward-reverse shock structure forms at its head. Any jet material that enters this structure via the reverse shock is heavily mixed. After the jet breaks out, the head material is pushed sideways and the jet is free to propagate uninterrupted. The mixing is then dominated by the R-T instability that develops above the collimation throat along the jet-cocoon interface. In a periodic jet the picture is different. The mixing of jet and stellar material is dominated by entrainment of ambient matter through the shock that forms at the head of each high-power shell, (see Figure 2 for models *E* and *G*), rather than by the formation of R-T instabilities at the collimation throat.

In models where each cycle of jet ejection is followed by a quiescent phase (*A*–*C*), we find that during each quiescent episode the cavity opened by the jet is filled by stellar material fast enough before the next cycle of jet material arrives. Consequently, a repeated forward-reverse shock structures (similar to the head in the continuous jet case) is formed at the front of each shell ejected in a new cycle, where the relativistic jet pushes upon the heavy stellar material. The mixing at these “heads” is high. Since the high-power shells do

<sup>1</sup> Since the 3D simulation box extends only up to  $5R_*$ , by the end of the simulation some of the fluid at the outflow front has propagated outside the box. The extension beyond  $5R_*$  shown in Fig 1 was obtained by extrapolating the 3D solution at earlier times to these radii.

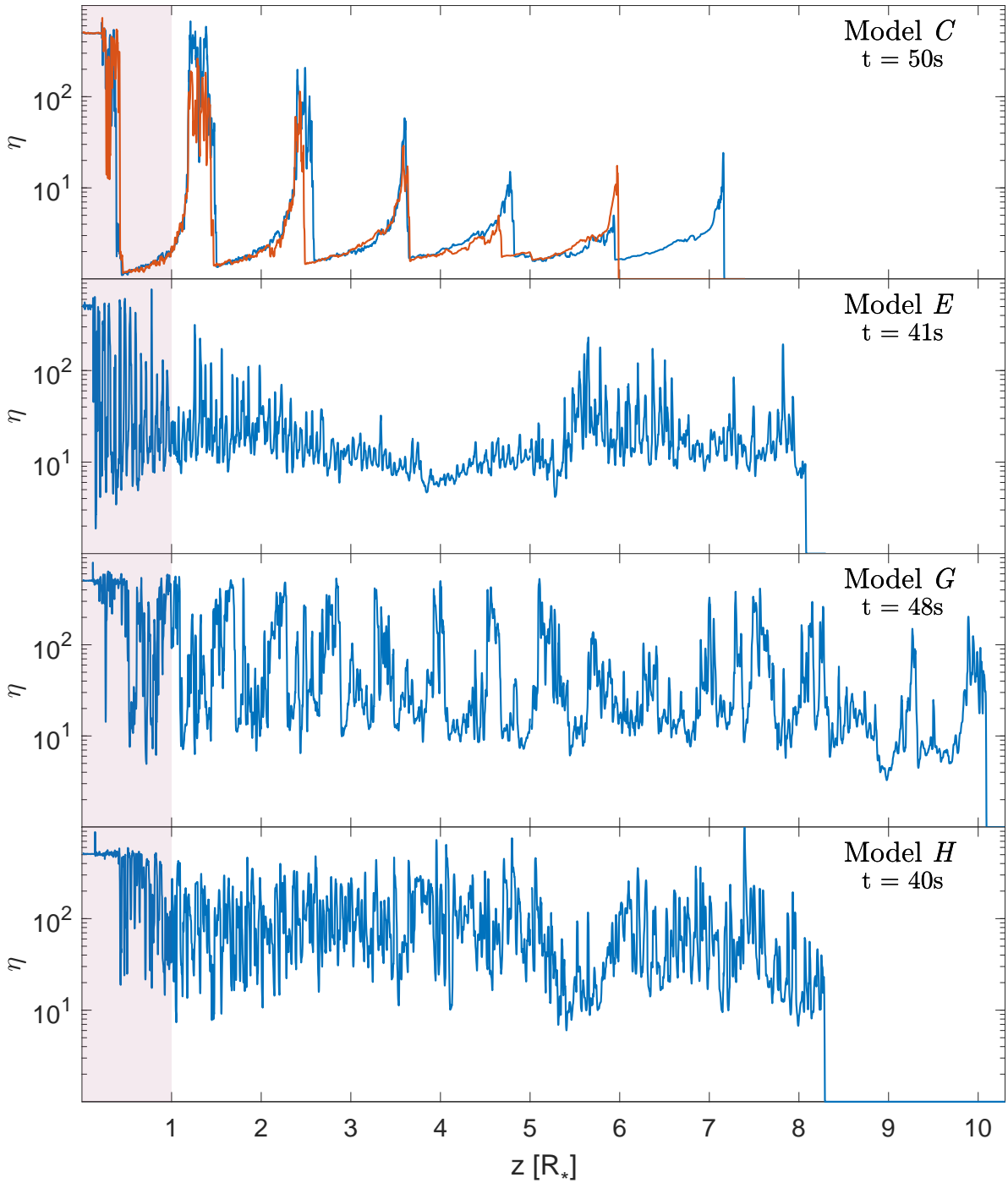


**Figure 1.** Profiles of  $\eta$  (the terminal Lorentz factor of each fluid element if it were propagating undisturbed to infinity) along the jet axis at the end of the 3D simulation for a sample of models. The indicated times are measured in the rest frame of the star. The pale red stripe marks the interior of the star. The red line in the top panel delineates the profile one duty cycle (4s) earlier than the blue line, indicating no evolution in time. Since our grid is stretched up to  $5R_*$ , the data at  $z > 5R_*$  is shifted from earlier times, assuming that no further mixing occurred.

not have sufficient energy to evacuate the large mass they encounter, they are choked in the dense medium early on, powering a non-relativistic expanding shock in the star. The mass enclosed inside the cavities between shells is dragged along with the outflow long after breakout occurs, as seen in the top panel of Figure 1 (low values of  $\eta$  indicate stellar material whereas high values correspond to the high-power shells). Ultimately, the fast shells decelerate, the slow

dense shells accelerate, and the entire outflow approaches a roughly uniform Lorentz factor. We find the mean Lorentz factor on the jet axis at the end of the simulation to be  $\langle \eta \rangle \equiv \int dE / \int dM \lesssim 10$  for models A – C, compared with  $\langle \eta \rangle \approx 90$  for the reference model H. The heavy baryon load of the intermittent jet renders the radiative efficiency at the photosphere to be practically zero in these models.

In models E, F and G (model D is found to be similar to model

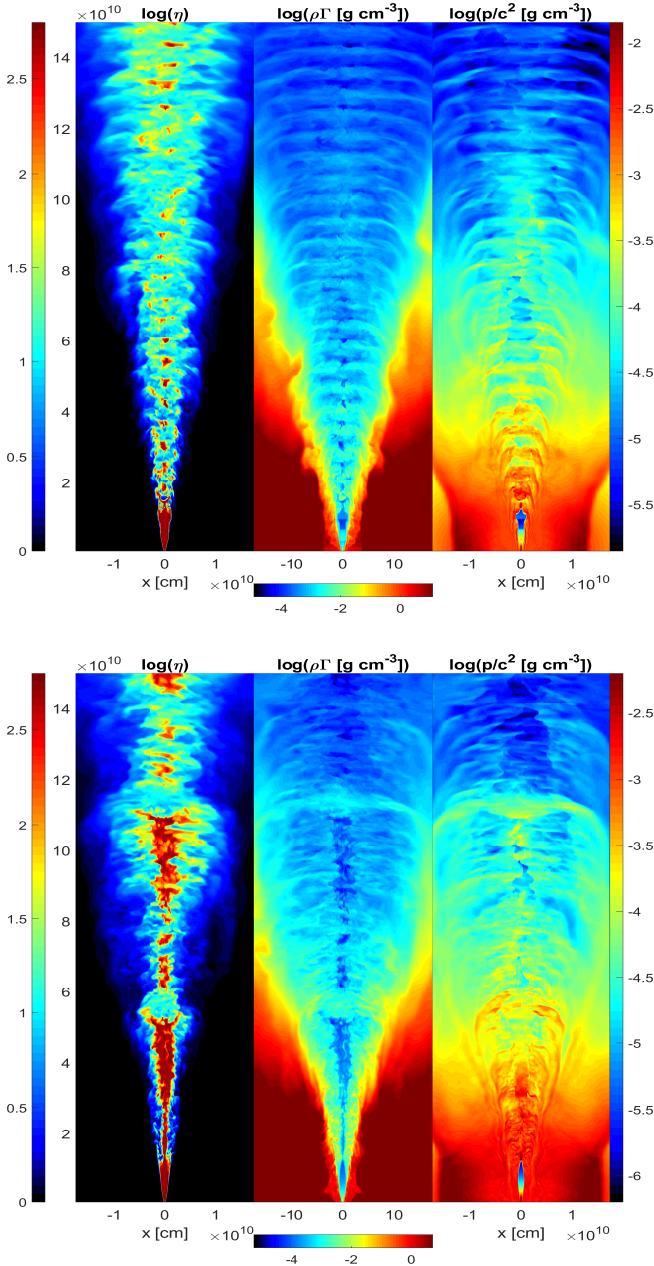


**Figure 2.** Maps of model *E* (top) and *G* (bottom) on plane  $x-z$  up to  $z = 1.5R_*$  at times 41s and 48s, respectively. Shown are  $\eta$  (left), mass density in the star frame (middle) and pressure (right). A video for model *E* is available at <http://www.astro.tau.ac.il/~ore/instabilities.html#modulations>.

*G*), where the jet power never falls below 10% of its maximal value, there are no quiescent phases during which stellar material can fill up the cavity in the jet. However, the modulation of the jet power leads to over-compression of low-power jet sections by the pressure in the cocoon, resulting, similarly to the cases where the jet has quiescent phases, in the formation of a forward-reverse shock at the head of each high-power shell that once again leads to mass entrainment (see Figure 2). For a given modulation amplitude, we generally find larger mixing at shorter modulation periods. The mean asymptotic Lorentz factor is  $\langle \eta \rangle \approx 15, 20$  and  $25$  for simulations *E, F*

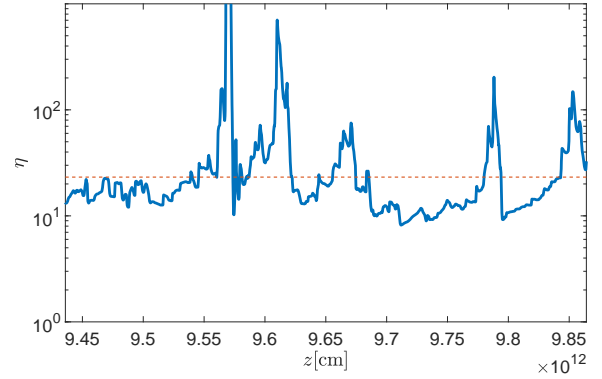


**Figure 3.** The  $\eta$  profile on the jet axis at the last snapshot of the 2D simulation of model *G*, when the jet head reaches  $z \approx 10^{13}$  cm. The back and the front of the jet are cut as they are subject to numerical artifacts. At  $z = 9.57 \times 10^{12}$  cm a small slab of matter shows a nonphysical behavior with  $\eta \approx 10^5$ . This slab of matter has a negligible amount of energy and thus does not affect the hydrodynamics. The dashed red line depicts the value of  $\langle \eta \rangle \approx 25$  of the shown jet elements.

and *G*, respectively; higher than in cases *A, B, C* but still significantly lower than that of the reference continuous jet in model *H*. We further find that internal shocks which are generated by collisions of slow and fast shells decay well below the photosphere, so that significant dissipation at or above the photosphere does not ensue in these models.

Figures 1 and 2 also show fast variations in  $\eta$  superposed on the periodic modulations in models *E* and *G*. These are caused by the instability of the collimating flow, as in the continuous jet model *H*. However, as stated above, loading by this process is sub-dominant. In principle, these variations can be imprinted in the resulting photospheric emission, however, as shown in the next section, the radiative efficiency in all modulated jet models is too small for the prompt emission to be detected.

In Figure 1 the fourth panel shows that at several stellar radii the flow in model *G* is rather inhomogeneous due to the intermittent nature of the jet engine, and that a non-negligible fraction of the outflow has high Lorentz factor ( $\gtrsim 100$ ). Over time, however, the internal shocks between fast and slow elements average out the hydrodynamic properties of the system, so that the flow becomes more homogeneous, approaching  $\langle \eta \rangle$  everywhere. In periodic jets, due to the low value of  $\langle \eta \rangle$ , these internal shocks take place far below the photosphere and therefore have a small contribution to the photospheric gamma-ray efficiency. Figure 3 depicts the  $\eta$  profile on the jet axis in model *G* when the jet head reaches  $z \approx 10^{13}$  cm. By this time the fast shocks have decelerated due to their interaction with the slow heavy elements. Consequently, the flow shown in the figure shows less variations between elements. At later times the flow will become even smoother by converging to the value of  $\langle \eta \rangle$  (dashed red line). We note that in the 2D simulation a numerical artifact leads to the formation of a slab with  $\eta \approx 10^5$ , as shown in the figure. This slab contains a negligible amount of energy and thus does not affect the hydrodynamics, and can be ignored in the radiation calculation in the next section.



## 4 EMISSION

### 4.1 Gamma rays

We calculate the radiative efficiency at the photosphere for models *E* and *G* for which we anticipate it to be the highest among the modulated jet models in table 1, since  $\eta$  has the largest values for these two models. The method employed is described in detail in GLN19. In short, in GLN19 we applied the fireball equations on the last snapshot of the simulation to extrapolate the evolution of each fluid element along radial streamlines up to its photosphere  $r_{ph}$ , defined as the location at which the radial optical depth to infinity is unity, that is,  $\tau(r_{ph}) = 1$ . The radiative efficiency of the fluid element is estimated to be the value of the quantity  $q = (h - 1)/h$  at  $r_{ph}$ , specifically  $\varepsilon = (h_{ph} - 1)/h_{ph}$ , where  $h$  is the enthalpy per baryon and  $h_{ph} = h(r_{ph})$ . This extrapolation ignores possible dissipation in sub-photospheric internal shocks, which was justified for the weak shocks generated by mixing in the continuous jet considered in GLN19 (model *H* in table 1). However, in models *E* and *G* the modulation of the engine gives rise to much stronger shocks. To properly account for the evolution of the flow in these cases we perform 2D simulations in a box that extends up to  $100R_*$ , where internal shocks decay, using the output of the 3D simulations as initial data for 2D simulations (see method in Gottlieb et al. 2018). Only above this radius we apply the extrapolation used in GLN19 to the photosphere. We note that the evolution of the outflow in the 2D simulations is followed for times much longer than the engine operation time, which in these runs is  $\sim 30$ s (the time it takes the jet to reach the outer edge of the 3D simulation box). As noted in the preceding section, we find that the evolution of newly ejected shells does not change much after this time, implying that the properties of the outflow computed below, and in particular the radiative efficiency, are representative also for prolonged engine activity.

The excessive baryon contamination in the intermittent jets pushes the photosphere of the outflow to radii significantly larger than those computed in the continuous jet model ( $\sim 10^{12}$  cm). We find that for most fluid elements the optical depth at the end of the 2D simulation (at  $r \simeq 10^{13}$  cm) is still large,  $\tau \sim 10^3$ . Using the extrapolation method developed in GLN19 beyond this radius yields  $r_{ph}$ . Figure 4a depicts the extrapolated photospheric radii of fluid elements on the jet axis for models *E* and *G*, showing that the photosphere of most fluid elements is located very far out, at  $z > 10^{14}$  cm. The horizontal axis gives the distance of jet elements in the last snapshot of the 2D simulation from the injection point; the shown slab (from  $\sim 9.4 \times 10^{12}$  cm to  $\sim 9.9 \times 10^{12}$  cm) constitutes the entire jet.

The photospheric radius thereby obtained is found to be much larger than the coasting radius of the jet,  $r_{coast} \lesssim 10^{12}$  cm. This readily implies very low radiative efficiency, as indeed confirmed by direct calculations. Figure 4b depicts the radiative efficiency of fluid elements on the jet axis in models *E* and *G* as a function of their location in the last 2D snapshot. As seen, the radiative efficiency of most fluid elements in both models is extremely low, with the exception of the section near the jet’s head, where the efficiency approaches  $\varepsilon \approx 10\%$ . The overall efficiency depends also on the relative energy carried by each fluid element, which is not shown in this plot. In fact, we find that the jet section where  $\varepsilon$  is highest contains only a small fraction ( $\sim 1\%$ ) of the total jet energy, hence its contribution to the net emission is small. To estimate the overall efficiency we average  $\varepsilon$  over the entire jet energy. Figure 4c shows the energy-weighted mean value of  $q$  on the jet axis as a function of the jet’s head location. The solid line in each model corresponds to the mean value of  $q$  in the 2D simulation data. The decline of  $\langle q \rangle$  with radius reflects gradual conversion of internal energy stored in shells

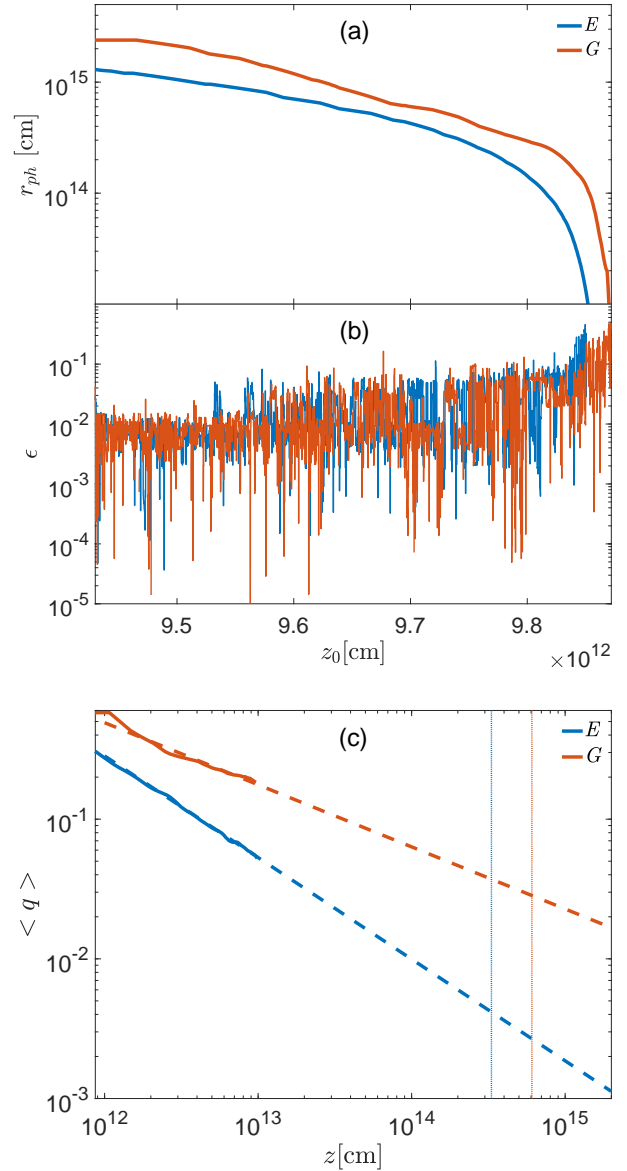


**Figure 4.** Photospheric radius (a) and radiative efficiency,  $\varepsilon = q_{ph} = (h_{ph} - 1)/h_{ph}$  (b), of fluid elements along the jet axis in models *E* and *G*, computed by extrapolating the data in the last snapshot of the 2D simulation. The horizontal axis gives the distance from the origin of each fluid element at the end of the 2D simulation. The shown slab (from  $\sim 9.4 \times 10^{12}$  cm to  $\sim 9.9 \times 10^{12}$  cm) is the entire jet. (c): Energy-weighted mean value of  $q = (h - 1)/h$  plotted as a function of the distance of the jet front from the origin. The solid lines delineate the values obtained from the 2D simulation. The dashed lines correspond to power-law extrapolation of the 2D data. The vertical dotted lines mark the energy-weighted mean photospheric radius in each model.

of high specific enthalpy (or high  $\eta$ ) to bulk energy of the heavily loaded shells (with low  $\eta$ ) through the decay of internal shocks. As explained above, the 2D simulation box does not extend all the way to the photosphere. Hence, in order to estimate the efficiency we extrapolated the  $\langle q \rangle$  profile obtained in the simulation (roughly a power law) to the energy-weighted mean photosphere (marked as the dotted vertical lines in the figure). The value of  $\langle q \rangle$  at  $r_{ph}$  is the energy-weighted efficiency  $\langle \varepsilon \rangle$ . As seen, the overall efficiency is a fraction of a percent in model *E* and about 2% in model *G*. This should be contrasted with continuous jet models for which

the overall efficiency was found to be high in GLN19. For the other intermittent jet models in table 1 the overall efficiency is expected to be much lower than in models *E*, *G*.

The above analysis suggests that an intermittent engine that expels a hydrodynamic outflow cannot produce a detectable  $\gamma$ -ray signal if its duty cycle is significantly shorter than the jet breakout time from the stellar envelope.

## 4.2 Afterglow

While intermittent hydrodynamic jets maintain a terminal Lorentz factor of a few dozens and will not produce a detectable  $\gamma$ -ray emission, they may still yield a detectable afterglow signal at later times as they interact with the external medium. Previously, GRB jets with high baryon loading, known as “dirty fireballs” (Dermer et al. 2000; Huang et al. 2002; Rhoads 2003; Lamb & Kobayashi 2017), have been suggested as the origin for an on-axis orphan afterglow (Nakar & Piran 2003).

Consider a relativistic jet with isotropic equivalent energy  $E_{\text{iso}}$  and terminal Lorentz factor  $\langle \eta \rangle$ , which propagates in an external medium with a density profile  $\rho(r) = \rho_a(r/r_i)^{-\alpha}$ . Our intermittent jet simulations show that  $\langle \eta \rangle \gtrsim 30$ , so that the reverse shock, which is formed from the interaction with the medium, is Newtonian (Nakar & Piran 2004). In such case the fireball equations dictate that the jet starts decelerating at radius

$$R_{\text{dec}} = \left[ \frac{E_{\text{iso}}(3 - \alpha)}{4\pi\rho_a c^2 \eta^2 r_i^\alpha} \right]^{\frac{1}{3-\alpha}}, \quad (1)$$

and the afterglow peak takes place at time

$$t_{\text{obs}} = \left[ \frac{(3 - \alpha)E_{\text{iso}}\eta^{8-2\alpha}}{2^{5-\alpha}\pi\rho_a c^{5-\alpha} r_i^\alpha} \right]^{\frac{1}{3-\alpha}} (1+z) \equiv A \left( \frac{E_{\text{iso},52}\eta_{200}^{8-2\alpha}}{\rho_{a,0}} \right)^{\frac{1}{3-\alpha}} (1+z), \quad (2)$$

where  $z$  is the redshift,  $E_{\text{iso}} = E_{\text{iso},52} \cdot 10^{52}$  erg and  $\eta = 200\eta_{200}$ . For a homogeneous medium ( $\alpha = 0$ ) the normalization is set as  $A \sim 14$  s. In such medium Equation (2) indicates that the afterglow peak time is delayed for lower Lorentz factors as  $t_{\text{obs}} \propto \eta^{-8/3}$ . That implies that for a given energy and density, plugging in the terminal Lorentz factor obtained in our simulations with  $L_{\text{min}} = 0$  postpones the afterglow onset time to  $\sim$  day after the jet launch. For the terminal velocities found when  $L_{\text{min}} > 0$ , the afterglow rises on  $\sim$  hour timescales.

The rate of on-axis orphan afterglows can be constrained by observations. Nakar & Piran (2003) have used X-ray fluxes to show that under the assumption that such dirty fireballs have similar energy per solid angle as regular GRBs, the rate of on-axis orphan afterglows cannot be much higher than that of typical GRB afterglows. Similar results were obtained by Ho et al. (2018) based on the lack of fast fading optical orphan afterglows in the iPTF survey. Orphan on-axis afterglows have possibly been observed before in the optical bands (e.g. Cenko et al. 2013), although it may be that in this case we just missed the  $\gamma$ -rays from this event due to the partial  $\gamma$ -ray sky coverage (at any time less than half of the sky is covered by sensitive  $\gamma$ -ray detectors). It is challenging however to differentiate on-axis orphan afterglows from off-axis orphan afterglows which emerge for regular GRB jets seen off-axis. It may be possible, however, to distinguish a dirty fireball from an off-axis orphan afterglow by the different contribution of the reverse shock during the rise of the afterglow (Sari & Piran 1999).

## 5 SUMMARY & DISCUSSION

The central engines of GRBs have long been considered to be intermittent, with duty cycles typically shorter than the outflow breakout time from the envelope of the collapsed star. The variability of the engine naturally leads to formation of strong internal shocks in the outflow that under appropriate conditions can dissipate a considerable fraction of the bulk energy near or above the photosphere. Such an activity has been commonly invoked to account for the nonthermal spectra and rapid variations of the prompt GRB emission although, as shown recently (GLN19), fast variability can also arise from sporadic mixing of jet and cocoon material even in cases of steady jet injection.

Since the photosphere is located well above the star, it is imperative to understand how a modulated jet evolves as it propagates through the envelope of the progenitor. In this paper we addressed this question by performing 3D simulations of hydrodynamic jets injected periodically from a small radius inside the star, for a range of modulation amplitudes and periods. By further evolving the outflow from the outer edge of the 3D simulation box (at  $5R_*$ ) to a much larger radius ( $100R_*$ ) using 2D simulations, we were able to compute the radiative efficiency of the flow.

We find, quite generally, that modulated jets with periods substantially shorter than the breakout time suffer excessive mass loading that strongly inhibits their emission. For all the models investigated, the radiative efficiency during the prompt phase never exceeded  $\sim 1\%$ , and in most cases is much smaller. This should be contrasted with emission from a continuous jet (steadily injected), that features highly efficient photospheric emission despite moderate mixing (GLN19). The excessive loading in the periodic jets is caused by dragging of stellar material by shocks that form at the interfaces between high and low power shells. Mixing by instabilities at the collimation zone, which is the primary loading mechanism in a continuous jet, is subdominant in the periodic jets.

Our results challenge the variable engine model for long GRBs. The question whether similar behavior is expected also in short GRBs (sGRBs) remains open. The combination of shorter breakout times and less massive medium surrounding sGRB jets is expected to mitigate the propagation of the relativistic jet through the medium. Therefore, the modulations considered here, of timescales which are comparable to the breakout times of sGRBs, may still yield an efficient GRB emission. However, if shorter duty-cycles lead to heavier loading, as found in our simulations, modulations of  $T \lesssim 10^{-2}$  s might provide similar results for sGRBs as well.

Our main conclusion is that intermittent hydrodynamic outflows cannot produce the observed prompt  $\gamma$ -ray emission, but may appear as X-ray, optical and radio transients that are similar to GRB afterglows starting hour to days after the GRB. Mild magnetization may alter these results, but it is not clear at present how. 3D RMHD simulations (Gottlieb et al. 2020) show that sub-dominant magnetic fields can suppress hydrodynamic instabilities in a continuous jet (see also Matsumoto & Masada 2019, for a qualitative discussion), thereby preventing significant mass loading of the jet. If this holds also in case of periodic jets, it could be that some critical magnetization is needed to produce a successful GRB. However, as we have shown the dominant loading process in periodic jets is not associated with hydrodynamic instabilities and, therefore, the results found for steady magnetized jets cannot be directly applied to intermittent jets. Attempts to perform 3D MHD simulations of periodic jets with mild magnetization are currently underway.

## ACKNOWLEDGEMENTS

This research was supported by the Israel Science Foundation (grant 1114/17). OG and EN were partially supported by an ERC grant (JetNS).

## REFERENCES

- Aloy M. A., Müller E., Ibáñez J. M., Martí J. M., MacFadyen A., 2000, *The Astrophysical Journal*, 531, L119
- Aloy M.-A., Ibáñez J.-M., Miralles J.-A., Urpin V., 2002, *Astronomy & Astrophysics*, 396, 693
- Beloborodov A. M., 2000, *ApJ*, 539, L25
- Centeno S. B., et al., 2013, *The Astrophysical Journal*, 769, 130
- Dermer C. D., Chiang J., Mitman K. E., 2000, *The Astrophysical Journal*, 537, 785
- Fenimore E. E., Ramirez-Ruiz E., Wu B., 1999, *The Astrophysical Journal*, 518, L73
- Geng J.-J., Zhang B., Kuiper R., 2016, *The Astrophysical Journal*, 833, 116
- Gottlieb O., Nakar E., Piran T., Hotokezaka K., 2018, *Monthly Notices of the Royal Astronomical Society*, 479, 588
- Gottlieb O., Levinson A., Nakar E., 2019, *Monthly Notices of the Royal Astronomical Society*, Volume 488, Issue 1, p.1416-1426, 488, 1416
- Gottlieb O., Bromberg O., Singh C. B., Nakar E., 2020, in prep.
- Gourgouliatos K. N., Komissarov S. S., 2018, *Monthly Notices of the Royal Astronomical Society: Letters*, Volume 475, Issue 1, p.L125-L129, 475, L125
- Ho A. Y. Q., et al., 2018, *ApJL*, 854, L13
- Huang Y. F., Dai Z. G., Lu T., 2002, *Monthly Notices of the Royal Astronomical Society*, 332, 735
- Lamb G. P., Kobayashi S., 2017, *Proceedings of the International Astronomical Union*, 12, 66
- Levinson A., Eichler D., 1993, *The Astrophysical Journal*, 418, 386
- Li H., Fenimore E. E., 1996, *The Astrophysical Journal*, 469, L115
- Lin D.-B., Lu Z.-J., Mu H.-J., Liu T., Hou S.-J., Lü J., Gu W.-M., Liang E.-W., 2016, *Monthly Notices of the Royal Astronomical Society*, 463, 245
- López-Cámara D., Morsony B. J., Lazzati D., 2014, *Monthly Notices of the Royal Astronomical Society*, 442, 2202
- Lopez-Cámara D., Lazzati D., Morsony B. J., 2016, *The Astrophysical Journal*, Volume 826, Issue 2, article id. 180, 8 pp. (2016), 826
- MacFadyen A., Woosley S. E., 1998, *The Astrophysical Journal*, Volume 524, Issue 1, pp. 262-289., 524, 262
- Matsumoto J., Masada Y., 2013a, *EPJ Web of Conferences*, 61, 02005
- Matsumoto J., Masada Y., 2013b, *The Astrophysical Journal Letters*, Volume 772, Issue 1, article id. L1, 6 pp. (2013), 772
- Matsumoto J., Masada Y., 2019, *MNRAS*, 490, 4271
- Matsumoto J., Aloy M. A., Perucho M., 2017, *Monthly Notices of the Royal Astronomical Society*, Volume 472, Issue 2, p.1421-1431, 472, 1421
- Matzner C. D., 2002, *MNRAS*, 345, 575
- McBreen B., Hurley K. J., Long R., Metcalfe L., 1994, *Monthly Notices of the Royal Astronomical Society*, 271, 662
- Meliani Z., Keppens R., 2010, *Astronomy and Astrophysics*, Volume 520, id.L3, 4 pp., 520
- Mignone A., Bodo G., Massaglia S., Matsakos T., Tesileanu O., Zanni C., Ferrari A., 2007, *The Astrophysical Journal Supplement Series*, 170, 228
- Morsony B. J., Lazzati D., Begelman M. C., 2007, *The Astrophysical Journal*, Volume 665, Issue 1, pp. 569-598., 665, 569
- Morsony B. J., Lazzati D., Begelman M. C., 2010, *ApJ*, 723, 267
- Nakar E., Piran T., 2002a, *Monthly Notices of the Royal Astronomical Society*, 330, 920
- Nakar E., Piran T., 2002b, *Monthly Notices of the Royal Astronomical Society*, 331, 40
- Nakar E., Piran T., 2003, *New Astron.*, 8, 141
- Nakar E., Piran T., 2004, *MNRAS*, 353, 647
- Norris J. P., Nemiroff R. J., Bonnell J. T., Scargle J. D., Kouveliotou C.,

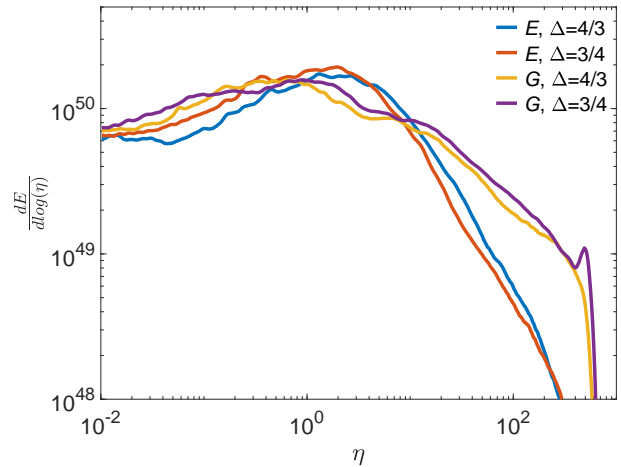


**Figure A1.** A comparison of distributions of the energy per logarithmic scale of  $\eta$  from simulations with different cells size  $\Delta$ .

- Paciesas W. S., Meegan C. A., Fishman G. J., 1996, *The Astrophysical Journal*, 459, 393
- Parsotan T., López-Cámara D., Lazzati D., 2018, *The Astrophysical Journal*, 869, 103
- Ramirez-Ruiz E., Fenimore E. E., 1998, *A&AS*, 138, 521
- Ramirez-Ruiz E., Fenimore E. E., 2000, *The Astrophysical Journal*, 539, 712
- Rhoads J. E., 2003, *The Astrophysical Journal*, 591, 1097
- Sari R., Piran T., 1997, *The Astrophysical Journal*, 485, 270
- Sari R., Piran T., 1999, *The Astrophysical Journal*, 520, 641
- Toma K., Komissarov S. S., Porth O., 2017, *Monthly Notices of the Royal Astronomical Society*, Volume 472, Issue 1, p.1253-1258, 472, 1253

## APPENDIX A: CONVERGENCE

We carry out convergence tests for simulations  $E$  and  $G$  as these the models which hold promise for producing the brightest electromagnetic signals. We perform two additional simulations for each model. One with a lower grid resolution, in which the cells size is  $4/3$  larger than the original size. And one of a higher resolution, in which the cells size is  $3/4$  the size of the original cells size. We test the convergence by comparing the energy distribution per a logarithmic scale of  $\eta$ , as depicted in Figure A1. Although the cells size in the two convergence simulations differ from each other by almost a factor of two, the distributions agree well with differences up to  $\lesssim 30\%$ . That implies that the results found in our simulations are qualitatively similar when increasing or decreasing the grid resolution.